university of groningen

University Medical Center Groningen

University of Groningen

Production of radioactive beams for atomic trapping

Traykov, Emil

IMPORTANT NOTE: You are advised to consult the publisher's version (publisher's PDF) if you wish to cite from it. Please check the document version below.

Document Version
Publisher's PDF, also known as Version of record

Publication date:
2006

Link to publication in University of Groningen/UMCG research database

Citation for published version (APA):
Traykov, E. (2006). *Production of radioactive beams for atomic trapping*. s.n.

Copyright
Other than for strictly personal use, it is not permitted to download or to forward/distribute the text or part of it without the consent of the author(s) and/or copyright holder(s), unless the work is under an open content license (like Creative Commons).

The publication may also be distributed here under the terms of Article 25fa of the Dutch Copyright Act, indicated by the "Taverne" license. More information can be found on the University of Groningen website: https://www.rug.nl/library/open-access/self-archiving-pure/taverne-amendment.

Take-down policy
If you believe that this document breaches copyright please contact us providing details, and we will remove access to the work immediately and investigate your claim.

Downloaded from the University of Groningen/UMCG research database (Pure): http://www.rug.nl/research/portal. For technical reasons the number of authors shown on this cover page is limited to 10 maximum.

Download date: 13-02-2023

Chapter 3

Thermalization of radioactive ions

The secondary beams from the magnetic separator have large transverse emittances and a wide energy distribution. Thermalization is required in order to efficiently collect the produced isotopes and transport them further as a beam of ions. Thermalization is based on the full stopping of the beam in matter for subsequent extraction. Such stopping devices are often called ion catchers.

This chapter gives an overview and comparison between the gas stopping technique and an alternative approach - the Thermal Ionizer (TI), which is used as an ion catcher in the TRIμP facility. Further, the theoretical description of the processes involved in a TI is given. The chapter concludes with a description of the design of the TI and commissioning experiments with ^{20}Na.

3.1 Gas cells

The basic principle of operation of gas stopper cells relies on slowing of the radioactive isotopes in gases to thermal energies due to multiple collisions with gas atoms/molecules. The thermalized ions drift in an electromagnetic field towards an aperture or nozzle where the ions exit with the flowing gas [Ärj85, Den97].

The size of the cell and the gas pressure depend on the energy distribution of the incoming ions. Narrowing of the energy distribution can be done to some extent with the range bunching technique. This technique requires an extra dispersive section and uses monoenergetic degraders [Wei00].

Stopping gas cells are currently in use at several nuclear facilities which include: MSU [Sch02, Wei04], ANL [Sav03], GSI [Neu04], JYFL [Den97, Äys01],

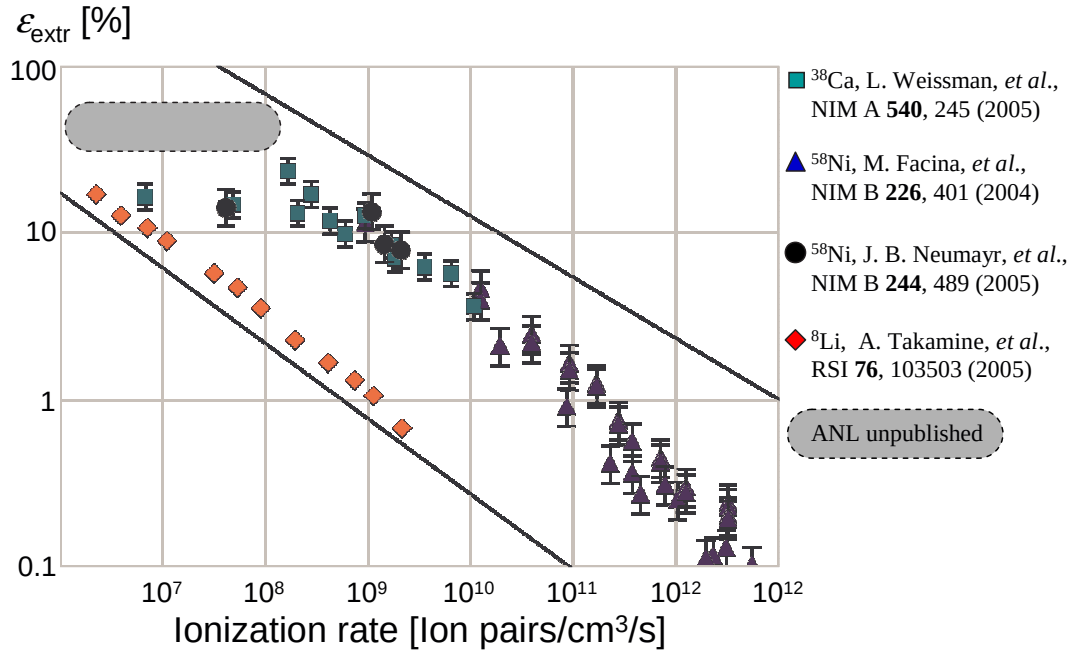

FIG. 3.1: Measured gas cell extraction efficiencies depending on the ionization rate in the gas volume. Figure adapted from [Mor06].

and KU Leuven [Kud01]. Slowing of ions using gas cells is considered also in future large-scale projects [FAIR, SPI2, RIA].

The gas cell stopper method is less dependent on the atomic properties of the isotope than methods that involve extraction from secondary ion sources where the chemical and physical properties are of great importance. The fast extraction ($<$ few ms) allows to utilize gas cells for stopping of a large variety of short-lived isotopes.

The main disadvantage of using gas cells is the transmission efficiency dependence on the ion beam intensity [Huy02B]. This dependence was confirmed in various experiments [Mor06] (Fig. 3.1). It is due to the creation of a high density of ion-electron pairs in the gas volume by the stopping of the ions. This creates a significant charge density in the gas volume resulting in screening of the electric fields and leading to an increase of the lateral distribution of the slowed ions.

Another gas cell parameter influencing the efficiency is the purity of the slowing gas. Impurities increase the probability for neutralization processes and molecule formation which lead to isotope losses. A recent study on gas stopping of ions in noble gases cooled to temperatures below 80 K confirmed the importance of gas purity [Den06]. The measurements showed a fast increase of the transport efficiencies from $\approx 2\%$ to $\approx 28\%$ for ^{219}Rn ions in helium with decreasing temper-

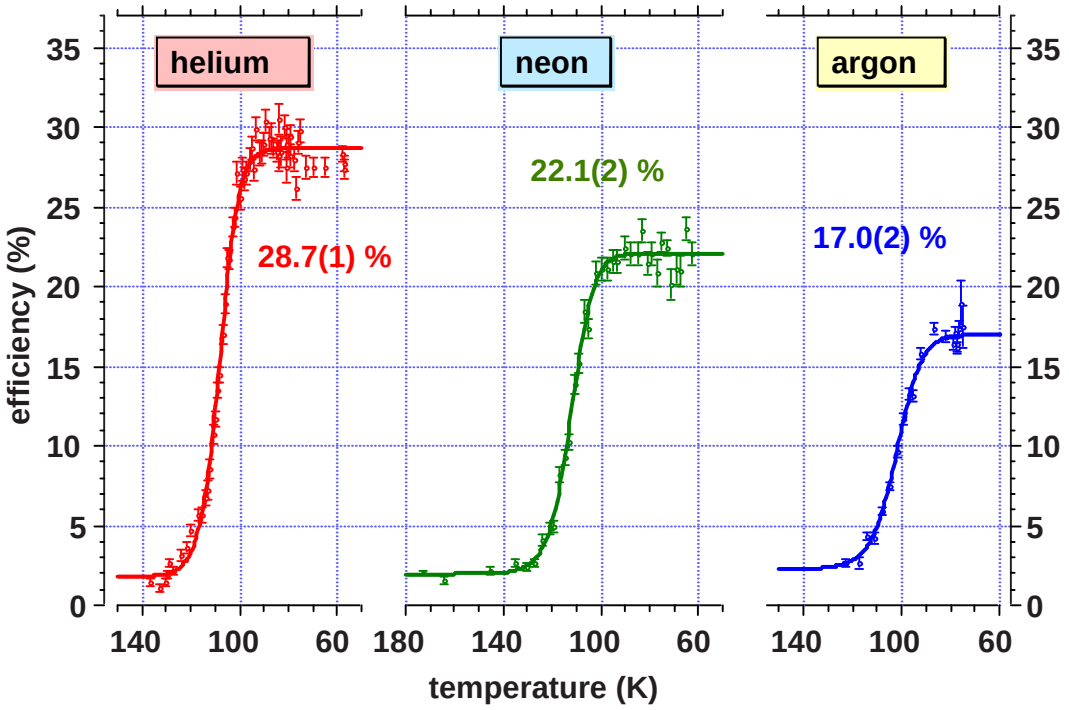

Fig. 3.2: Temperature dependence of transport efficiencies for ^{219}Rn ions in helium, neon, and argon. Figure adapted from [Den06].

ature. The highest efficiencies were measured in the temperature region below 90 K where most of the oxygen freezes out from the gas volume. Similar results were obtained for neon and argon gases in the same temperature range (Fig. 3.2). The maximal efficiencies reached at low temperatures are probably related to charge changing cross sections and may represent the fundamental upper limits for the efficiencies for given ion-gas combinations [Den06].

Neutralization and stripping cross sections for various ions in different noble gases were measured at KVI [Wil06]. The measurements were made below 1 keV/u ion energy where few data are available. The setup consisted of a differentially pumped gas target at pressures that allow only a few collisions between the ion and the gas atoms. The average charge of the ions decreased to below 1 for ion momenta below $50 \cdot 10^8$ cm u/s (Fig. 3.3). The results show that charge-exchange during stopping of ions in noble gases is not governed only by the ionization potential of the gas. Neutralization prior to stopping will occur and reionization is required in order to obtain high ionization efficiencies at thermalization.

A gas cell suitable for slowing of a large range of isotopes was initially considered as an ion catcher for the TRIμP facility, but the difficulties with the extraction efficiency discussed above led to the decision to use an alternative

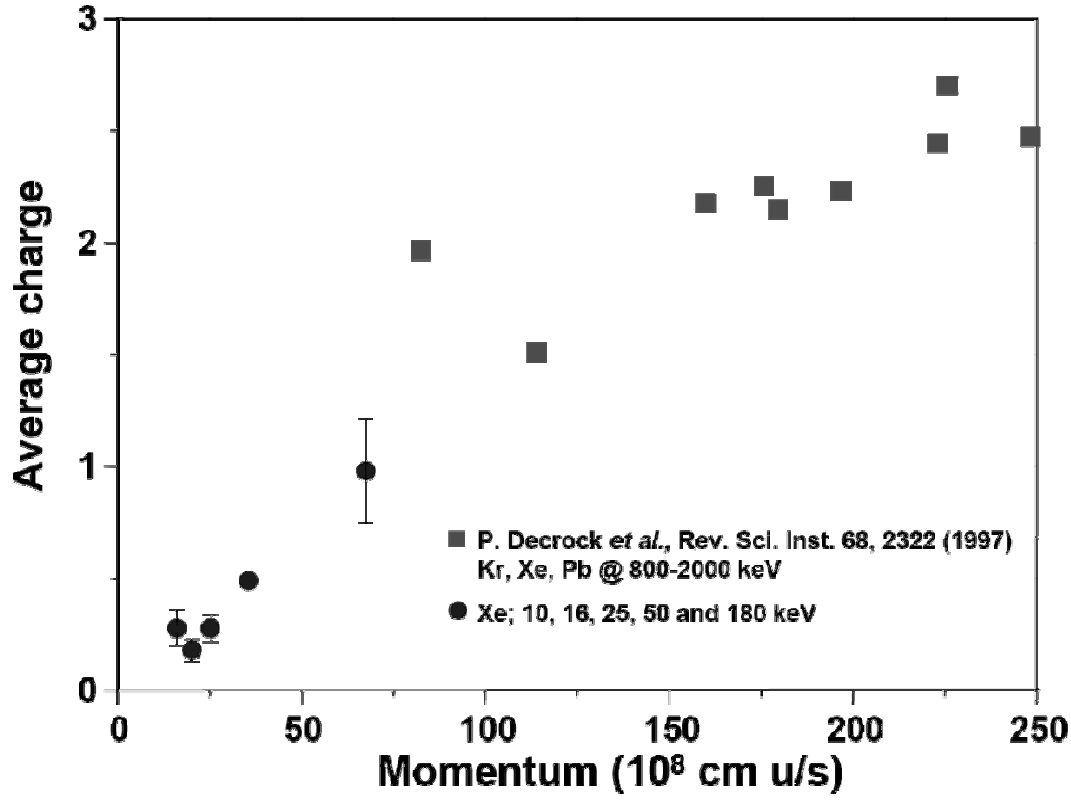

FIG. 3.3: Average charge state of ions passing through helium at different momenta. Figure adapted from [Wil06].

method based on a Thermal Ionizer (TI) [Kir81], since the efficiency of the TI does not depend on the secondary beam intensity. Similar devices are used in ISOL (Isotope Separation On-Line) facilities as targets and secondary ion sources for production and extraction of radioactive isotopes.

An important reason to choose a TI as an ion catcher is the expected high efficiency for alkaline and alkaline-earth elements (including Na and Ra) which are important for the primary physics goals of TRIμP (Section 1.2). The range of elements suitable for extraction with the TI also includes the elements for which atomic trapping is technically achievable.

The main difference between the design of the TI for TRIμP and the ISOL design is that the radioactive isotopes are produced outside the TI instead of using the device as the production target which often requires thick targets and large dimensions. The dimensions of the TRIμP TI are defined only by the energy distribution of the ions at the end of the magnetic separator. This keeps the dimensions of the Thermal Ionizer small providing fast extraction and, thus, high total efficiencies for short-lived isotopes. Advantageous in the case of the

TRIμP Thermal Ionizer is the possibility for easy handling and modification of the setup because activation is negligible.

3.2 Thermal ionizers

The basic operation of the Thermal Ionizer can be divided into several consecutive parts: stopping, diffusion, effusion, ionization, and extraction. The main parts of the TRIμP Thermal Ionizer setup are shown schematically in Fig. 3.4. Ions are stopped in tungsten foils which are placed in a tungsten cavity. In the experiments reported here a stack of 9×1.5 μm foils was used. The total thickness of the foils covers the range distribution of the isotopes, considering the energy distribution at the end of the separator. The isotopes stopped in the foils move to the surface of the foils by diffusion. This process is enhanced by heating the foils of the cavity to high temperatures. At the foil surface the isotopes can escape. Multiple collisions occur with the cavity walls and the ion-electron plasma inside the cavity volume. During collisions the charge state of the isotope may change many times. An electric field gradient formed by a DC potential on the extraction electrode allows extraction of the ions through the exit aperture. The extraction thus requires the isotopes to be ionized. Isotopes leaving the aperture as atoms will be lost.

Heating of the cavity is done by electron bombardment from surrounding W filaments heated by an electric current. The electrons are guided towards the tungsten cavity surface by applying a DC electric potential ($\sim$ 600 V). In order to concentrate the heat to the inner parts, several heat shields are used surrounding the cavity. At the temperature of the inner cavity the main heat transfer mechanism is radiation while in regions at lower temperature conduction is dominant. Water cooling of the outer heat shields is used to keep the vacuum chamber at room temperature. The thickness of the heat shields upstream of the cavity have to be taken into account in the stopping calculation. The Thermal Ionizer requires a tungsten cavity operating at temperatures above $\sim$2500 K, which is technically challenging. Operation at such high temperature requires appropriate design and material choices. In order to reach sufficient temperatures but prevent overheating, readout and control of the temperature is required. Operation at high temperatures limits the lifetime of the heated parts, for example the cavity walls and filaments, which requires that provisions for maintenance of these parts should be considered in the design.

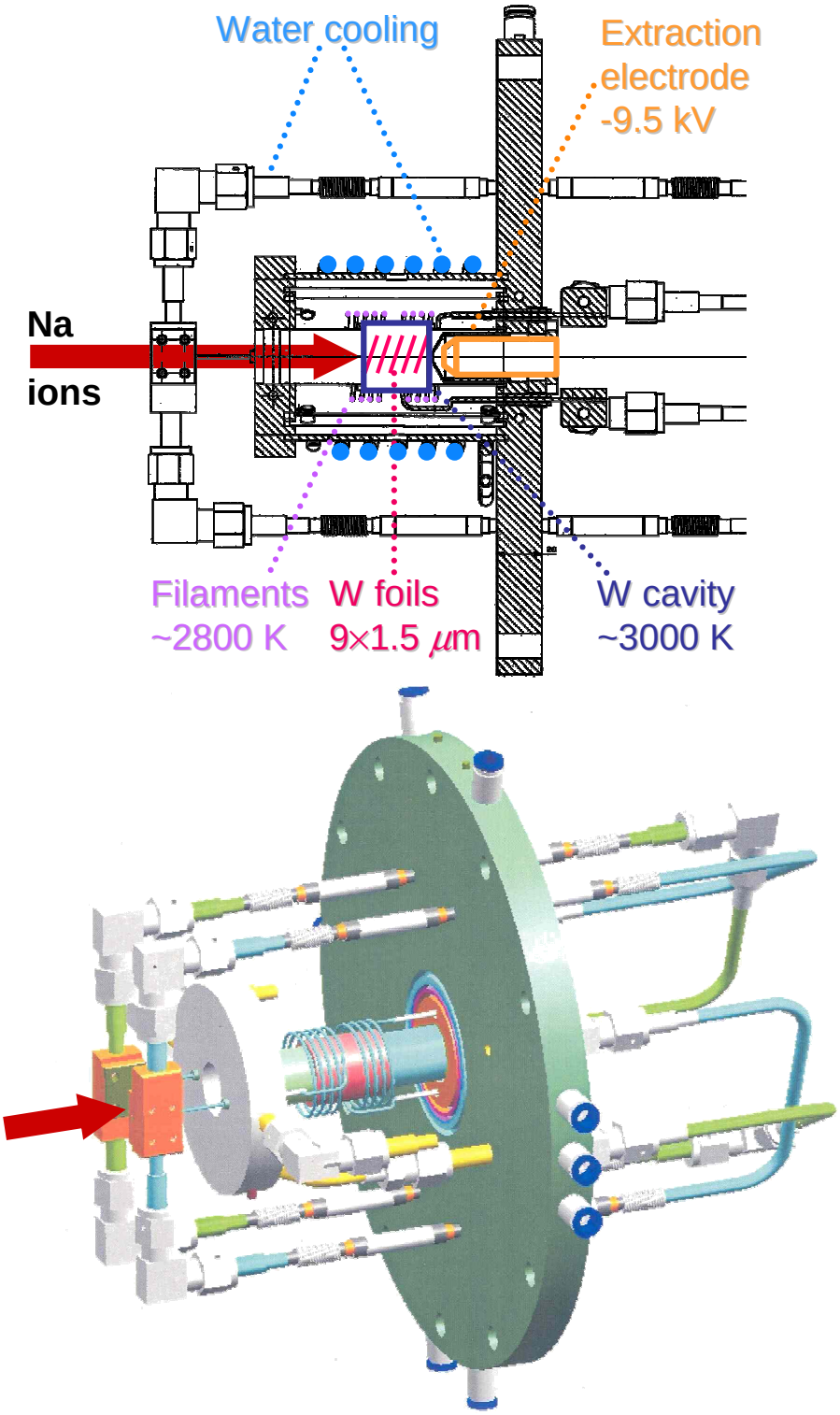

FIG. 3.4: Schematic of TRIμP Thermal Ionizer.

3.2.1 Stopping of ions in solids

The radioactive isotopes have high energies when leaving the separator. A rotatable degrader is placed close to the Final Focal Plane (FFP) of the separator that is used for fine adjustment of the stopping range in the tungsten foils of the Thermal Ionizer. The rotatable degrader system used for the Thermal Ionizer commissioning measurements consisted of a 40 μm Al foil. Downstream from the degrader there are three tungsten foils with thicknesses 55, 4, and 4 μm that also act as heat shields of the Thermal Ionizer. The mean magnetic rigidity and corresponding energy of the ions are obtained from the settings of the bending magnets in the second section of the separator. The energy distribution is calculated taking into account the energy acceptance of the separator and the additional widening due to straggling effects from the slowing in degraders and foils. There are 9 tungsten stopping foils each with a thickness of 1.5 μ. Thickness inhomogeneities are taken into account for the estimate of the final stopping range distribution.

3.2.2 Diffusion of ions in solids

When the desired isotopes are stopped inside the Thermal Ionizer foils they have to come to the surface by diffusion. The diffusion process is governed by the diffusion equation [Cha43], which can be derived from Fick's laws [Fic55] and the continuity equation

$$\frac{\partial C}{\partial t} = D\nabla^2 C(\vec{r}, t), \tag{3.1}$$

where C is the concentration of the diffusing particles per unit volume at a given position $\vec{r}$ in the foil at time t and D is the diffusion coefficient, which is considered to be constant in the foil.

The steady state diffusion (Fick's first law), i.e. when the concentration of the particles C does not change in time, is given by

$$\vec{j} = -D\nabla C(\vec{r}), \tag{3.2}$$

where $\vec{j}$ is the flux of the particles at any position $\vec{r}$ inside the foil volume.

The diffusion constant D depends on the material temperature T

$$D(T) = D_0 e^{-\frac{E_0}{RT}}, \tag{3.3}$$

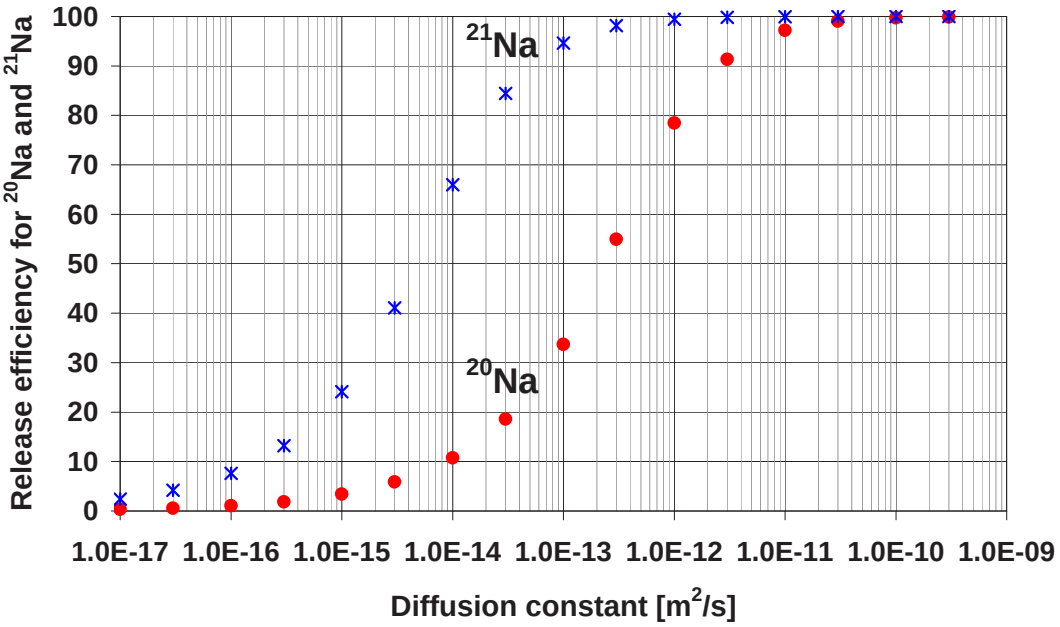

FIG. 3.5: Calculation of the fractional release efficiencies for ^{20}Na and ^{21}Na ions from a 1.5 μm foil for different diffusion constants (Eq. 3.4). The efficiencies represent the fraction of isotopes which would reach the surface within one half-life, for ^{20}Na and ^{21}Na this is 448 ms and 22.5 s, respectively.

where D_0 and E_0 are the Arrhenius coefficients for diffusion, representing the maximum diffusion constant D for $T \rightarrow \infty$ and the activation energy for diffusion, respectively.

Analytical solutions of the diffusion equation [Cra79, Fuj81] for an infinite foil with a thickness d lead to the fractional release efficiency after a time t (assuming homogeneous deposition of the isotopes and extraction from both surfaces)

$$\varepsilon_d(t) = 2\sqrt{\frac{tD}{d^2}}\tanh\left(\sqrt{\frac{d^2}{4tD}}\right), \tag{3.4}$$

which allows one to estimate efficiencies in case of radioactive isotopes by substituting t with $T_{1/2}$, which is the half-life of the radioactive isotope. The release efficiency curve for ^{20}Na ($T_{1/2} = 0.448$ s) and ^{21}Na ($T_{1/2} = 22.5$ s) and a 1.5 μm thick foil is plotted versus the diffusion constant $D(T)$ in Fig. 3.5.

Measured data for $D(T)$, D_0, and E_0 are available for a large variety of elements and materials. Diffusion data for sodium in tungsten could not be found in the literature, however data exist for lithium and potassium in tungsten [McC60, Lov63, Bay83, Kir92], as well as, data for lithium, and potassium in various refractory metals [Kla66, Kir92, Del02] and sodium in platinum [Kla66].

Estimation for diffusion of sodium in tungsten was done by scaling of diffusion data for other alkaline metals in tungsten [Sch58]

$$\frac{D(M_1)}{D(M_2)} \propto \sqrt{\frac{M_2}{M_1}}, \tag{3.5}$$

where $D(M_1)$ and $D(M_2)$ are the diffusion constants for isotopes with mass M_1 and M_2, respectively. The scaling can be done both for the diffusion constants $D(T)$ at a given temperature.

Data for diffusion coefficients D_0 and E_0 and constants $D(T)$ from the literature are listed in Tables 3.2.2 and 3.2.2. The data vary by orders of magnitude for the same isotope in the same lattice. The reason for that is probably in the differences in the details of the experiments. Often the substructure of the host material is not taken into account and the surface diffusion or grain boundary diffusion are measured instead of lattice diffusion. For the Thermal Ionizer lattice diffusion should be considered since the ions are implanted mainly inside the grains.

Element	Material	D_0 [m^2/s]	E_0 [kJ/mol]	T range [K]	Reference
Li	Tantalum	$2.0{\cdot}10^{-9}$	145	1423 - 1773	[Kla66]
Li	Tungsten	$8.2{\cdot}10^{-3}$	234	1000 - 1400	[McC60]
Li	Tungsten	$3.5{\cdot}10^{-4}$	170	1365 - 1500	[Lov63]
K	Tungsten	$3.0{\cdot}10^{-5}$	44	1000 - 1673	[Bay83]
K	Tungsten	$3.0{\cdot}10^{-5}$	73	1000 - 1673	[Bay83]
K	Rhenium	$3.0{\cdot}10^{-4}$	517	2200 - 2300	[Del02]
Li	Platinum	$5.0{\cdot}10^{-7}$	222	1423 - 1773	[Kla66]
Na	Platinum	$5.5{\cdot}10^{-5}$	290	1423 - 1773	[Kla66]

Table 3.1: Arrhenius coefficients D_0 and E_0 for alkaline elements in refractory metals and platinum derived from measured diffusion constants in a given temperature range.

Values of $D(T)$ for ^{20}Na obtained by scaling (Eq. 3.5) are shown in Table 3.2.2. The results differ by a few orders of magnitude leading to a large uncertainty in the estimation of the diffusion delay related efficiency (Fig. 3.5).

An unexpected behavior can be observed from the diffusion data showing varying diffusion values at high temperatures [Kir92]. The reason for that may be that diffusion mechanisms change with temperature [Kir92, Bey03].

Time-dependent fractional release profiles for sodium diffusion in tungsten foils were obtained also using the diffusion part of the Monte Carlo code Radioactive Ion Beam Optimizer (RIBO) [San05]. The program can be used for

Element	Material	$D(T)$ [m^2/s]	T [K]	Reference
Li	Tantalum	$1.2{\cdot}10^{-13}$	1773	[Kla66]
K	Tantalum	$3.3{\cdot}10^{-13}$	2550	[Kla66]
K	Tantalum	$3.0{\cdot}10^{-14}$	2550	[Kla66]
Li	Tungsten	$2.4{\cdot}10^{-13}$	1160	[McC60]
K	Tungsten	$7.2{\cdot}10^{-13}$	2600	[Kir92]
K	Tungsten	$4.0{\cdot}10^{-15}$	2600	[Kir92]
K	Rhenium	$3.0{\cdot}10^{-16}$	2250	[Del02]
Li	Platinum	$2.1{\cdot}10^{-13}$	1773	[Kla66]
Na	Platinum	$3.0{\cdot}10^{-14}$	1773	[Kla66]

TABLE 3.2: Diffusion constants for alkaline elements in refractory metals and platinum measured at different temperatures.

Element	Material	$D(T)$ [m^2/s]	T [K]	Reference
Na	Tungsten	$1.4{\cdot}10^{-13}$	1160	[McC60]
Na	Tungsten	$1.0{\cdot}10^{-12}$	2600	[Kir92]
Na	Tungsten	$5.7{\cdot}10^{-15}$	2600	[Kir92]

TABLE 3.3: Diffusion constants for sodium (Eq. 3.5) estimated from diffusion data for lithium and potassium (Table 3.2.2).

calculations of various parameters involved in the extraction of ions from ISOL targets including diffusion, effusion, and ionization processes.

The diffusion mechanism described here does not include the desorption delay due to the time needed for the ions to leave the surface and the probability for the ions to re-diffuse inside the stopper foils. Desorption time depends on the desorption enthalpy ΔH_D for a given ion and material [Eic79]. Alkaline and alkaline-earth elements have very low ΔH_D values which allows one to neglect the desorption delay and re-diffusion.

3.2.3 Effusion

After diffusion to the surface of the stopper foils the elements have to be transported to the Thermal Ionizer exit. The process of extraction of the elements from the cavity to the exit aperture is called effusion. During effusion the products undergo multiple collisions with stopping foils and cavity walls and interactions

with plasma. The frequency of the latter depends on the mean free path inside the TI cavity, thus on the background pressure.

The mean delay time for effusion τ_e is defined as the sum of the total time spent between collisions with walls and the total time the ions spent on the walls due to adsorption

$$\tau_e = \chi(\tau_f + \tau_a), \tag{3.6}$$

where τ_f is the average time between collisions with the walls, τ_a is the average "sticking time", and χ is the mean number of collisions before leaving the exit aperture.

The average time between collisions with material surface τ_f is calculated from the temperature of the system defining the energy of the particles

$$\tau_f(T) = l\sqrt{\frac{M}{2kT}}, \tag{3.7}$$

where l is the mean distance between materials (estimated by the size of the cavity and the distance between the foils), M is the mass of the isotope, and k the Boltzmann constant. The average adsorption time τ_a, which also depends on the temperature T, is governed by the Frenkel equation

$$\tau_a(T) = \tau_0 e^{-\frac{H_a}{RT}}. \tag{3.8}$$

Here $1/\tau_0$ is the frequency factor ($\tau_0 \approx 10^{-13}$ s), H_a the partial molar adsorption enthalpy, and R the universal gas constant. Adsorption enthalpy H_a and sticking time τ_a for different materials are given in Table 3.2.3. In the operation range of the TRIμP Thermal Ionizer, T from 2200 to 3000 K, the values for τ_a range from $1.0{\cdot}10^{-10}$ to $1.6{\cdot}10^{-11}$ s, respectively.

The mean number of collision χ_1 can be estimated for neutral particles by the ratio of the total area of materials inside the cavity (walls and stopping foils) A_c and the exit aperture area A_a. The exit aperture of the TRIμP TI has a diameter of 0.30 cm ($A_a \approx 0.071$ cm^2). The total surface area is $A_c \approx 155$ cm^2 giving an estimate for the number of collisions, $\chi_1 \approx 2000$.

For charged particles this estimate is not valid because of penetrating electric fields through the aperture from the extraction electrode. The estimation in that case can be done by the ratio of the total cavity volume A_c and A_e which is the area inside the cavity where the electric potential is equal to the thermal energy of the ions kT. In order to estimate A_e, the Thermal Ionizer has been

Element	Material	T_{melt} [K]	ΔH_a [kJ/mol]	τ_a [s]	T_{exp} [K]
Na	Pt	2042	130.0	$8.2{\cdot}10^{-10}$	1735
Na	Mo	2896	80.2	$5.0{\cdot}10^{-12}$	2462
Na	Ta	3290	125.4	$2.2{\cdot}10^{-11}$	2797
Na	Re	3459	184.9	$1.9{\cdot}10^{-10}$	2940
Na	W	3695	127.1	$1.3{\cdot}10^{-11}$	3141
Al	W	3695	431.8	$1.5{\cdot}10^{-6}$	3141
Si	W	3695	616.8	$1.8{\cdot}10^{-3}$	3141
C	W	3695	888.3	$5.9{\cdot}10^{+1}$	3141

TABLE 3.4: Enthalpy of adsorption ΔH_a and sticking time τ_a measured at different temperatures T_{exp} for sodium on different materials [Ros84].

modeled in the program Femlab [Zim04] and electric potentials inside the cavity were calculated (Fig. 3.6). Equipotential lines corresponding to -0.1 V, -0.2 V, -0.3 V, and -0.4 V are indicated in the plot. The ion energy at $T = 2300$ K is 0.2 eV and 0.3 eV at $T = 3500$ K corresponding to A_e of 1.14 and 0.85 cm^2, respectively. The mean number of ion collisions in the cavity at $T = 2300$ K and at $T = 3500$ K was calculated to be $\chi_2 \approx 136$ and $\chi_2 \approx 182$, respectively.

Since $\chi_1 \gg \chi_2$, the maximal effusion delay can be estimated using χ_1. Effusion delay times were obtained for $\chi_1 = 2000$ and $T = 2000$ K resulting in $\chi_1\tau_f = 2.4$ μs, $\chi_1\tau_a = 0.5$ μs, and the mean effusion delay $\tau_e = 2.9$ μs. Both τ_f and τ_a decrease with further increase of the temperature. The obtained results are many orders smaller than the lowest estimated delay from the diffusion in the stopping foils and, for sodium extraction from the TRIμP Thermal Ionizer, effusion delay can be neglected. This is due to the very low adsorption enthalpy (and corresponding sticking times) for sodium on tungsten. In case of other isotopes, for example aluminium, silicon, and carbon (Table 3.2.3), the delay due to effusion is comparable or greater than diffusion related delay and should not be neglected.

3.2.4 Ionization and beam formation

The isotopes have to be ionized in the Thermal Ionizer in order to be extracted as an ion beam. Extraction is done by applying a negative electric potential on the extraction electrode shown in Fig. 3.6.

The main ionization mechanism is surface ionization which occurs during ion

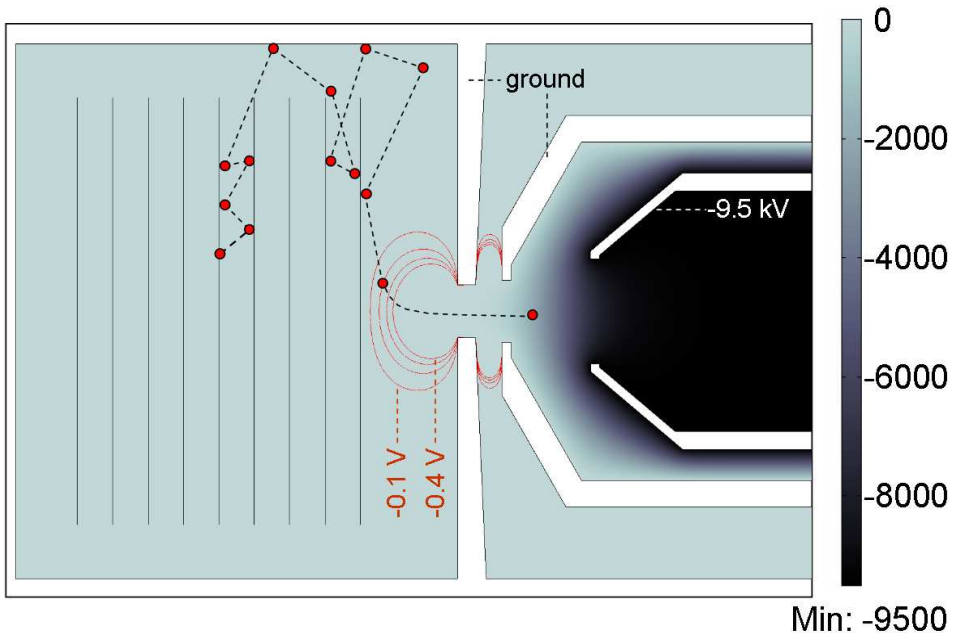

Fig. 3.6: Calculation of electric potentials inside the TI cavity created by setting the TI extraction electrode to -9.5 kV. Equipotential lines are shown for U= -0.1, -0.2, -0.3, and -0.4 V. A schematic trajectory of an ion is shown in the plot.

collisions with ionizer walls. Charge-changing processes in the ionizer volume, i.e. not at the surfaces, can be neglected due to low probabilities depending on the mean free path λ of the ions/atoms inside the ionizer volume and the ionization potentials of the elements inside the cavity. At lower TI operation temperatures (below $\sim$ 2500 K) the background pressure stays below $\sim 10^{-4}$ mbar and λ (taking an upper limit for the interaction radius of $\sim 10^{-9}$ m) is several orders higher than the mean distance between the cavity walls and the stopping foils (< 3 mm). At temperatures $\gtrsim$ 2500 K the vapor pressure in the tungsten cavity increases significantly and λ can be of the order of 1 mm thus collisions in the volume should be taken into account.

The degree of surface ionization α_s is completely given by the Langmuir equation [Lan25]

$$\alpha_s = \frac{n_{is}}{n_{as}} = \frac{g_i}{g_0} \exp\left(\frac{\varphi - W_i}{kT}\right), \tag{3.9}$$

where n_{is} and n_{as} are the ion and atom densities, respectively, evaluated near the cavity surface. They can be considered uniform in the whole cavity volume at low temperatures. g_i and g_0 are the statistical weights of the ionic and atomic states, respectively, obtained from the total angular momentum of the states $J_{i,0}$

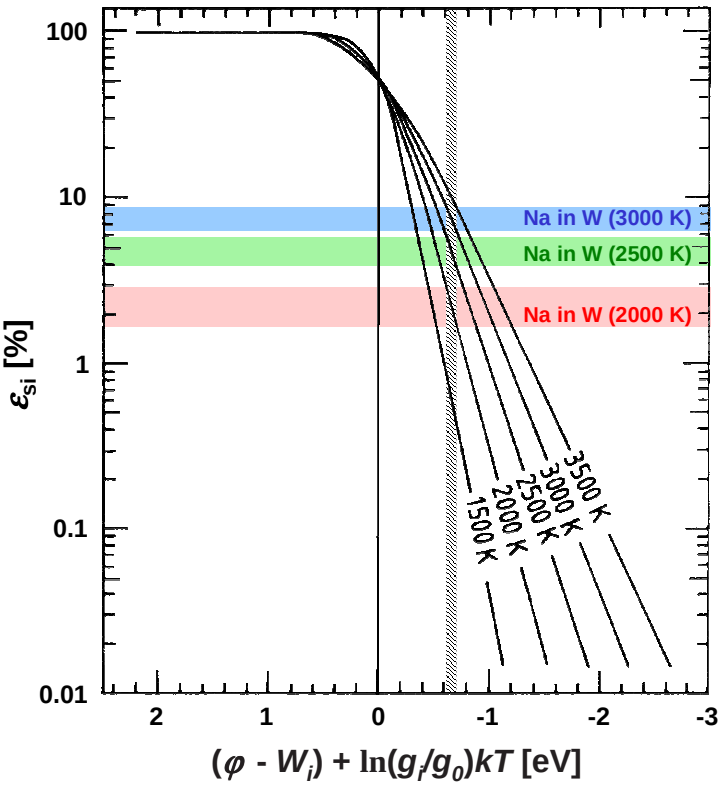

FIG. 3.7: Dependence of surface ionization efficiency ε_{si} on $\varphi - W_i$ plotted for various surface temperatures. Original figure adapted from [Kir81]. Additional horizontal dotted stripes are estimates of the surface ionization efficiencies for sodium in tungsten cavity at different temperatures $T = 2000$, 2500, and 3000 K. The vertical dotted stripe represents the difference $\varphi - W_i \approx -0.7$ eV which is estimated including corrections for $g_i/g_0 = 0.5$. The temperature dependence of φ of tungsten has different values in literature which are included in the estimation.

(g_i/g_0=1/2 for alkali elements). φ and W_i are the work function of the ionizing material and the first ionization potential of the element of interest, respectively. The surface ionization efficiency is then

$$\varepsilon_{si} = \frac{n_{is}}{n_{is} + n_{as}} = \frac{\alpha_s}{1 + \alpha_s}. \tag{3.10}$$

Fig. 3.7 shows the surface ionization efficiencies as a function of $\varphi - W_i$ (corrected for the statistical weights) for different temperatures T. The ionization efficiency for sodium on a tungsten surface is calculated to be between 1 to 9 % for T in the range from 2000 to 3000 K. The uncertainty of the tungsten work function φ dependence on the temperature T is taken into account in the calculation. The surface ionization efficiency for sodium on tungsten surface was

measured to be in the range from 6 to 8 % in the temperature range from 2200 to 2850 K [Dat56].

At higher temperatures ($\gtrsim$2400 K for W) the ionization efficiency increases due to the "hot cavity" effect related to the formation of quasineutral plasma in the cavity volume [Lat75, Afa77, Kir81, Kir90]. This effect is explained below.

The tungsten cavity of the TRIμP Thermal Ionizer is heated by electron bombardment from two tungsten filaments outside the cavity. Thermionic emission is quantified by the Richardson's law [Ric21]

$$J = A_0 T^2 \exp\left(-\frac{\varphi}{kT}\right), \tag{3.11}$$

where J is the current density, T and φ the material temperature and work function, respectively, and $A_0 = 4\pi m_e e k^2/h^3 = 120.2$ AK^{-2}cm^{-2} is the Richardson's constant (m_e is the electron mass). Electrons are emitted also from the tungsten stopping foils and the inner walls of the cavity. The density of electrons n_{es} at the tungsten surface is

$$n_{es} = 2\left(\frac{2\pi m_e k}{h^2}\right)^{3/2} T^{3/2} \exp\left(-\frac{\varphi}{kT}\right), \tag{3.12}$$

where h is Planck's constant. At temperatures above ~2100 K the electron density $n_{es} \approx 10^9$ cm^{-3} becomes comparable with the ion density n_{is} from the surface ionization of the elements in the cavity (mainly tungsten vapour and alkaline impurities). With further increase of the temperature both n_{es} and n_{is} increase, but the density of the emitted electrons from the surface surpasses by few orders the total ionic density n_i. At these densities the electrons, ions, and atoms form a quasineutral plasma in the cavity volume ($n_i \approx n_e$) while the majority of the electrons are concentrated near the tungsten surface and form a potential wall resulting in a negative potential U_{plasma} inside the cavity volume.

The quasineutrality assumption is valid when the Debye length λ_D of the charged particles is smaller than the distances between the walls and the stopping foils inside the cavity

$$\lambda_D = \sqrt{\frac{\varepsilon_0 kT}{n_e e^2}}, \tag{3.13}$$

where ε_0 is the vacuum permittivity, n_e is the density of the electrons inside the plasma. A calculation for the TRIμP Thermal Ionizer at $T = 2100$ K and $n_e \approx n_i \approx 10^9$ cm^{-3} results in $\lambda_D = 0.1$ mm which decreases further with increasing charged particle densities.

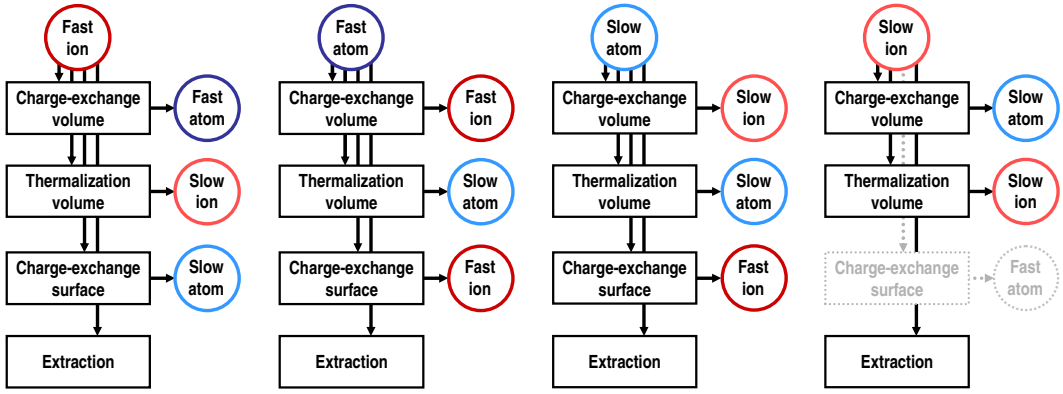

FIG. 3.8: Block diagram illustrating element states and processes in the Thermal Ionizer operating in the hot cavity regime.

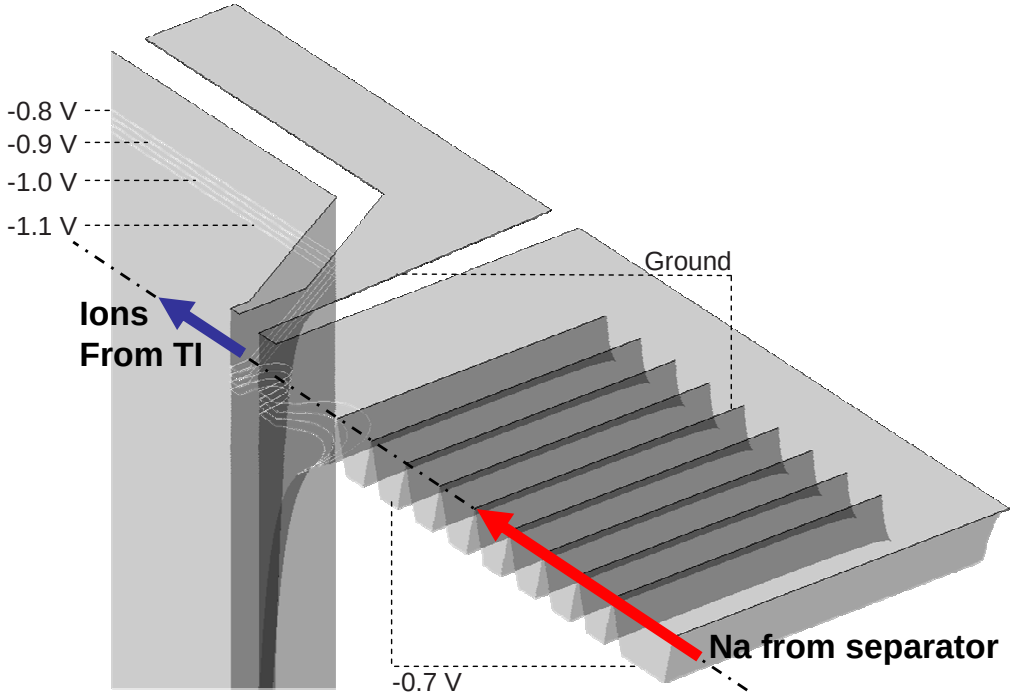

FIG. 3.9: Electric potential calculation inside the TI volume including the formation of a plasma potential (U_{plasma} = -0.7 V at T = 2500 K) which increases the kinetic energy of the ions in the TI volume. The height represents the electric potential in the plot. All surfaces remain at ground potential. Ions leaving the cavity surface at ground potential accelerate due to the plasma potential formed near the surfaces. If an ion collides with a thermalized particle in the volume, the kinetic energy of the ion is reduced and the ion cannot reach a surface and stays trapped in the volume. Atoms leave the surface without being accelerated (at thermal energies) and if ionization occurs in the volume the resulting ions will be trapped in the plasma potential as well. These two mechanisms lead to the increase of the ionization efficiency (hot cavity effect).

The plasma potential U_{plasma} due to the excess of electrons at the surface is given by

$$U_{plasma} = \frac{kT}{e} \ln\left(\frac{n_i}{n_{es}}\right). \tag{3.14}$$

Data from off-line measurements with the Thermal Ionizer of the vapour pressure dependence on the cavity temperature were used for the estimation of the sum of the neutral and ionic densities, n_0 and n_i, and the corresponding n_{is} for surface ionization of Na from equation 3.9. The measured background pressures are due to tungsten material evaporation and the outgassing impurities, mainly sodium, potassium, aluminium, and calcium, of which only potassium has a lower ionization potential $W_i(\mathrm{K}) = 4.34$ eV than sodium. A strict upper limit on n_i can be used by assuming that the measured pressure is entirely due to ionized vapour ($n_i \approx n_0 + n_i$). The corresponding plasma potential U_{plasma} for $T = 2200$ K and $T = 2500$ K was calculated to be -0.2 V and -0.7 V, respectively.

The negative plasma potential acts as a trap for thermalized positive ions which prevents wall collisions of the ions from the plasma. This increases the total degree of ionization α by an "amplification factor" N compared to the degree of surface ionization

$$\alpha = N\alpha_s = N\frac{g_i}{g_0} \exp\left(\frac{\varphi - W_i}{kT}\right), \tag{3.15}$$

and

$$N \leq N_{TE} = \frac{n_{es}}{n_i} = \exp\left(\frac{-eV_p}{kT}\right), \tag{3.16}$$

where N_{TE} is the maximal amplification which can be obtained in case of thermal equilibrium, i.e. when the elements are held sufficiently long in the cavity volume. The processes related to the hot cavity effect are illustrated in Fig. 3.8 and an electric potential calculation in the TI taking into account the plasma potential ($U_{plasma} = -0.7$ V) is shown in Fig. 3.9.

The thermal equilibrium condition is not fulfilled (and not desired for short-lived isotopes) for the Thermal Ionizer due to the presence of an exit aperture allowing ions and atoms to leave the cavity. The probability for ion thermalization increases with plasma density. This is done either by increasing Thermal Ionizer temperature or by filling the cavity with low pressure noble gas [Kir90]. In practice, the amplification factor N can not surpass the mean number of wall collisions of the ions χ_A. Typically, N is a few times smaller [Kir90] (Fig. 3.10).

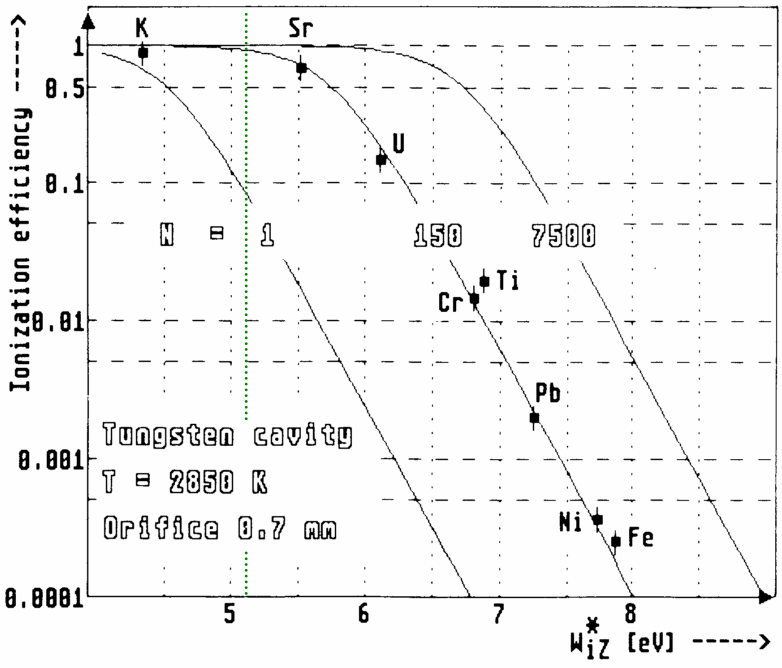

FIG. 3.10: Ionization efficiency amplification in hot cavities [Kir90]. For the given ionizer design at $T = 2850$ K the amplification factor N is estimated to be 150 from measured efficiencies for various ions (squares). Figure adapted from [Kir90].

The extraction efficiency ε_{extr} is increased compared to the ionization efficiency ε_i due to the presence of a penetrating electric field through the exit aperture of the cavity. The amplification is equal to the ratio χ_1/χ_2 and the resulting extraction efficiency is

$$\varepsilon_{extr} = \frac{\chi_1}{\chi_2}\varepsilon_i. \tag{3.17}$$

The amplification χ_1/χ_2 is ≈ 16 for the TRIμP Thermal Ionizer at 2300 K which means that high extraction efficiencies ($\gtrsim 80$ % for $\varepsilon_i \gtrsim 5$ %) are even expected below the temperature range for the hot cavity effect.

3.3 The Thermal Ionizer for TRIμP

3.3.1 Design and specifications

The Thermal Ionizer was designed as an ion catcher for alkaline and alkaline earth elements [Der05]. The material of choice for the cavity walls and stopping foils is tungsten because of its high working temperature allowing utilization of

the hot cavity (plasma) ionization. In addition, diffusion and effusion related delays are highly reduced at high temperatures which is beneficial for short-lived isotopes. The main parts, the tungsten cavity and stopping foils, the electron bombardment heating system, the heat shields, the water cooling of the chamber, and the electrostatic extraction are shown in Fig. 3.4. The dimensions of the main cavity elements are listed in Table 3.3.1.

Cavity length	25	mm
Cavity diameter	30	mm
Stopping foils diameter	25	mm
Stopping foils thickness	1.5	μm
Distance between foils	1	mm
Number of foils	9	
Entrance windows thickness	62	μm

Table 3.5: Main elements of the Thermal Ionizer. All elements are made of tungsten.

Platinum was used as an alternative material for the ion stopping foils. The main advantage of platinum is its high work function $\varphi = 5.65$ eV provides high ionization efficiencies for surface ionization at lower temperatures. Efficiencies for ionization of sodium on tungsten and platinum surfaces were measured some time ago [Dat56]. The surface ionization efficiencies for sodium on tungsten are $\lesssim 8$ % in the temperature region below 2850 K, whereas an efficiency of 84 % is reached for platinum at 1700 K. The diffusion constant for sodium in platinum was measured at 1773 K in [Kla66], $D(1773) = 3 \cdot 10^{-14}$ m^2/s. The lower melting point of platinum (2045 K) compared to tungsten (3683 K) is the main limiting factor to achieve fast release from the foils which makes platinum not suitable as a stopper for short-lived isotopes despite the high ionization efficiency, as was found empirically.

Different materials for the stopping foils and the cavity walls can be used for optimizing diffusion and ionization separately. However, possible deposition and monolayer formation on the cavity walls from evaporated stopping material will influence the ionization properties and should be considered in such designs.

3.3.2 Experimental setup

The main goals of the first measurements with the Thermal Ionizer were to verify the operation principles of diffusion, effusion, and ionization in the hot cavity and

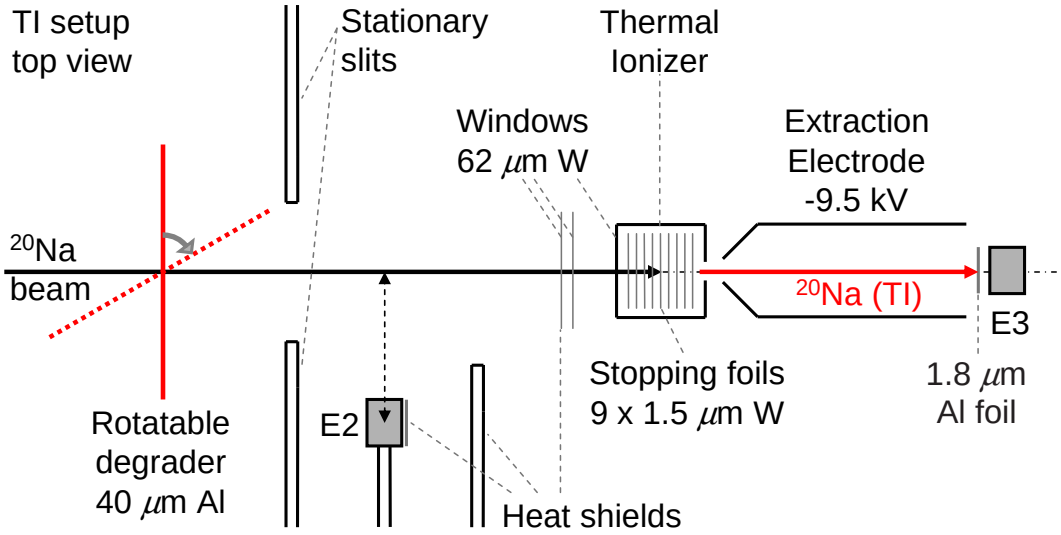

FIG. 3.11: A schematic of the Thermal Ionizer setup.

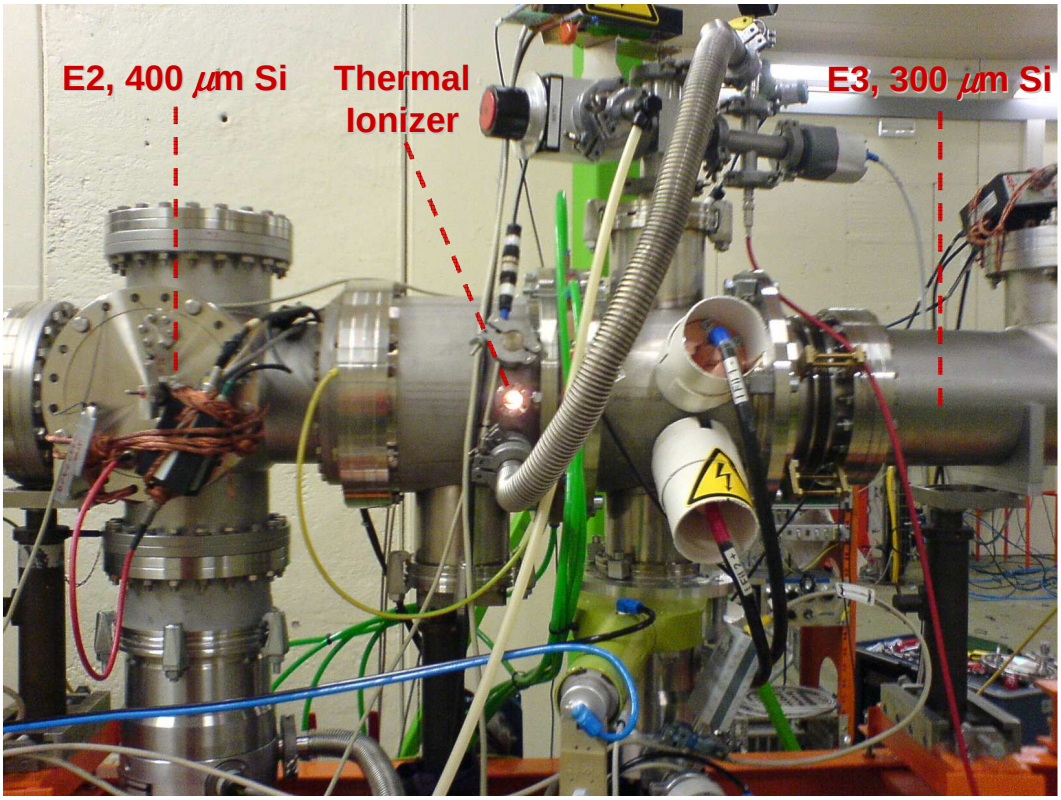

FIG. 3.12: Photograph of the experimental setup used for the commissioning measurements with the TRIμP Thermal Ionizer. Secondary isotope beam direction is from left to right.

to draw conclusions about critical design parameters for future improvements of the setup.

The isotope used for the commissioning measurements was ^{20}Na ($T_{1/2}$ = 448 ms). Its production and separation were described in Chapter 2. The experimental setup of the Thermal Ionizer is shown in Fig. 3.11 and 3.12. The positions of various parts are indicated. The detector upstream of the Thermal Ionizer, $E2$, is a silicon detector used for $\Delta E - TOF$ measurements to identify and optimize the incoming current of the produced isotopes. The detector $E3$ is positioned behind the extraction electrode of the Thermal Ionizer to measure the rate of delayed α particles from the β-decay of ^{20}Na. The branching ratio for the α decay is 16.37 $\pm$ 1.28 % [Til98]. A 1.8 μm thick aluminium foil is placed in front of $E3$ in order to stop the ions extracted from the Thermal Ionizer and detect the alpha-particles from the decay of ^{20}Na. The decay of ^{20}Na has been studied and the alpha lines and branching ratios are well known [Cli89].

3.3.3 Measurements of ^{20}Na stopping and extraction

Stopping and identification of ^{20}Na

After production and separation in the magnetic separator, the next step is to ensure that the isotope of interest, ^{20}Na, stops in the foils of the Thermal Ionizer. A total of 9 foils of 1.5 μm thickness and 2.5 cm diameter mounted on a tungsten frame were used. The mean energy of the ions was determined by the magnetic rigidity settings of the magnets. To allow varying of the implantation depth a rotatable 40 μm Al degrader was used for fine adjustment of the energy of the incoming ions. In this way the maximum of the stopping range distribution can be adjusted to the center of the stopping foils.

Four different magnet settings were used in the commissioning measurements. Two of the settings correspond to the forward and backward peaks of the ^{20}Na distribution as discussed in Chapter 2. These two settings differ by $\approx$ 5 % in momentum. The other two settings used a 30 μm Al degrader in the Intermediate Focal Plane (IFP) of the separator to change from "stopping mode" (inside the Thermal Ionizer foils) to "shoot-through" mode (implantation in $E3$). In shoot through mode the decay lines of the α particles from the decay of the implanted ^{20}Na were observed in $E3$.

Even in the stopping mode a fraction of the ^{20}Na beam ($\lesssim$ 1 %) is not stopped in the Thermal Ionizer foils due to range straggling and passes through the exit

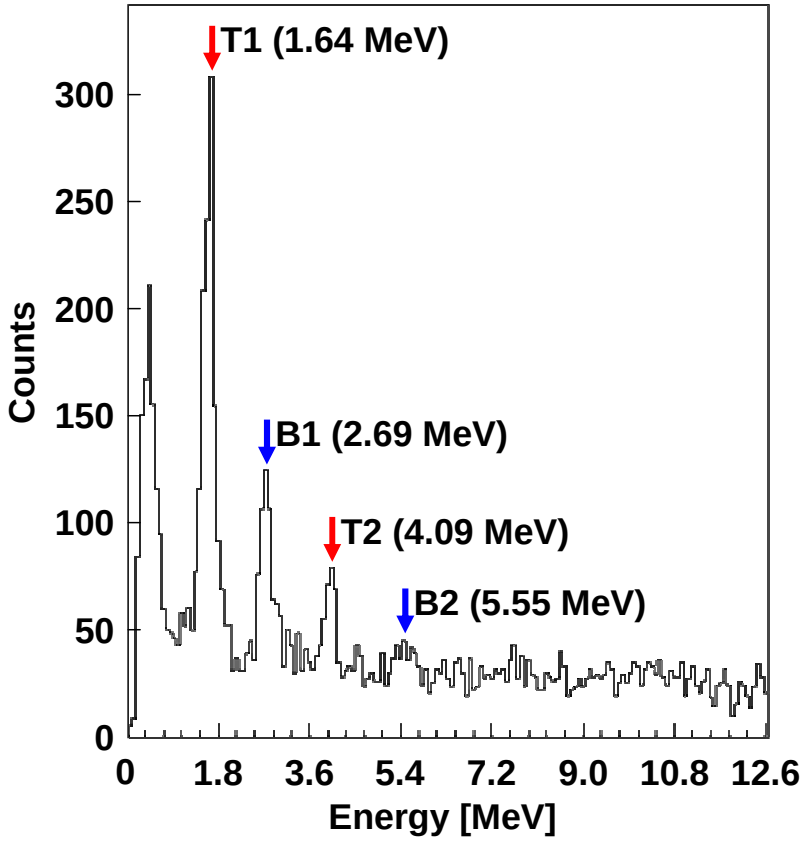

FIG. 3.13: Characteristic lines from α particles following ^{20}Na β-decay. Lines B1 and B2 are obtained from implantation of ^{20}Na ions in detector E3 (secondary beam passing through the Thermal Ionizer). Lines T1 and T2 are from ^{20}Na ions extracted from the Thermal Ionizer, accelerated to $\approx$ 9.5 keV, and implanted in a 1.8 μm Al foil in front of E3.

aperture of the TI. These ions are implanted in the detector E3 where the full energy of the α decays is measured (peaks B1 and B2 in Fig. 3.13). The ^{20}Na ions released from the TI are stopped in the 1.8 μm Al foil upstream of E3, and only the energy of the emerging α particles is measured in E3 (peaks T1 and T2). The origin of the α lines was found by turning off the extraction voltage which made the TI related lines (T1 and T2) disappear while the lines from the tail of the ^{20}Na distribution (B1 and B2) were seen independent of the extraction voltage.

Operation of the Thermal Ionizer

The TI efficiency measured for different ionizer temperatures is shown in Fig. 3.14. Initially, the cavity was heated by radiation from the filaments.

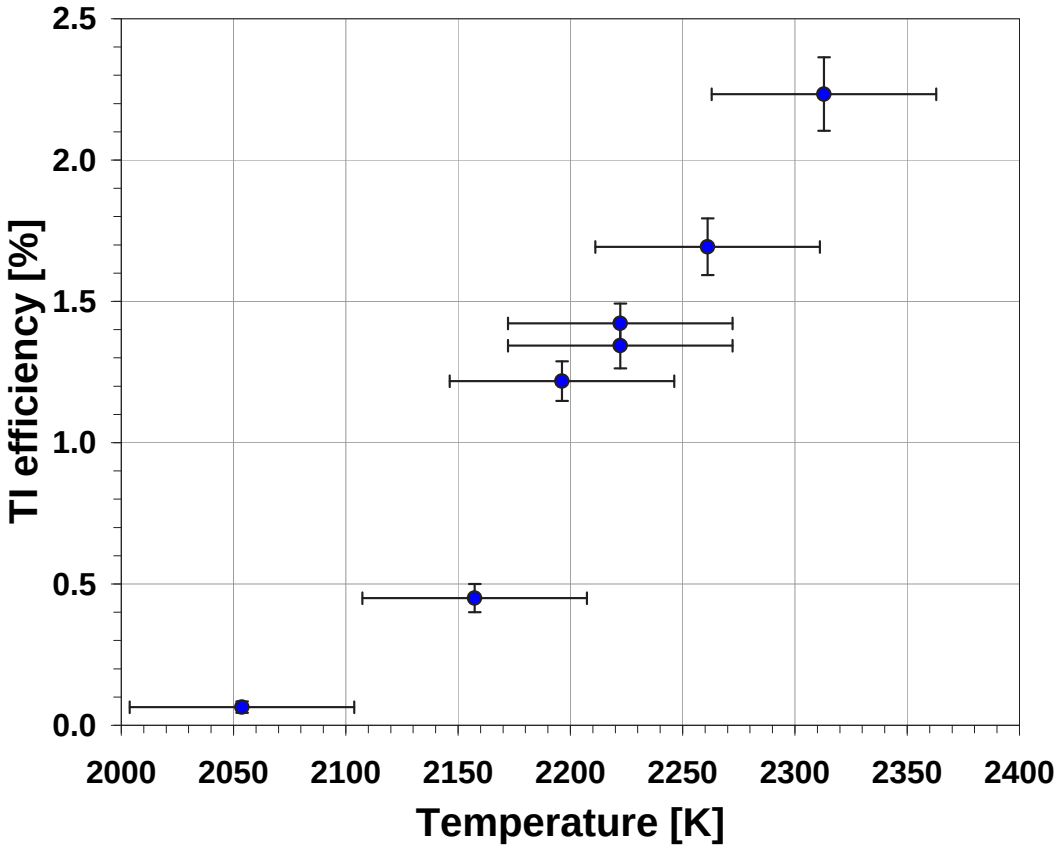

Fig. 3.14: Temperature dependence o the TI extraction efficiency obtained by measuring deposited energy in detector E3 from ^{20}Na decay related α particles.

The temperature of the Thermal Ionizer was increased by adjusting the current through the electron emitting filaments. The α particles from the decay of the extracted ^{20}Na ions from the Thermal Ionizer were detected first at $T \approx 2000$ K with the corresponding TI efficiency $\varepsilon_{TI} = 0.009$ %. Their rate was increased ≈ 25 times at 2250 K ($\varepsilon_{TI} = 2.3$ %) due to decreased diffusion delay and increased ionization efficiency. The TI efficiency is obtained by measuring the ratio between the count rate R_{TI} of ^{20}Na ions stopped in the foil in front of E3 and the count rate R_{total} of ^{20}Na in E2

$$\varepsilon_{TI}(^{20}\mathrm{Na}) = \frac{R_{TI}}{R_{total}}. \tag{3.18}$$

R_{TI} is obtained from the measured rate of α particles $R_{TI}(\alpha)$ in E3 taking into account the branching ratio (16.37%) and the acceptance reduction (18%) due to the solid angle Ω determined by the distance between the 1.8 μm Al foil and the detector $E3$.

3.3.4 Summary and outlook

The TI efficiency for ^{20}Na can be used to estimate the efficiency for ^{21}Na taking into account the half-lives of the isotopes.

Surface ionization is dominant at temperatures below 2500 K and the associated ionization efficiency is $\approx 3\%$ at 2000 K and $\approx 6\%$ at 2300 K (Eq. 3.10 and Fig. 3.7). The extraction efficiency is estimated to be ≈ 16 times higher than the ionization efficiency due to the penetrating field inside the cavity (Section 3.2.4), reaching a value of $\gtrsim 90\%$ at 2300 K. The extraction efficiency and the calculated diffusion release curves in Fig. 3.5 can be used to estimate the efficiency of the TI for ^{21}Na in the same temperature region. A 2.3% TI efficiency for ^{20}Na corresponds to 16% for ^{21}Na.

The design temperatures for optimal operation of the Thermal Ionizer were not reached due to electric short-cuts of the filaments at high temperatures. Correction will require a modification of the support of the filaments. The efficiencies are expected to be significantly increased at higher temperatures due to shorter diffusion times and the increasing significance of the hot cavity effect. Currently, an improved Thermal Ionizer is being built and will be tested. A large number of thinner stopper foils will be used and higher operation temperatures are expected.